Size effects on high temperature oxidation of MCrAlY coatings processed via APS and HVOF depositions

Ali Kalush, Damien Texier, Maxime Ecochard, Quentin Sirvin, Karim Choquet, Thomas Gheno, Nicolas Vanderesse, Walid Jomaa, Philippe Bocher

Size effects on high temperature oxidation of MCrAlY coatings processed via APS and HVOF depositions

Ali Kalush[a], Damien Texier[b,*], Maxime Ecochard[b], Quentin Sirvin[b], Karim Choquet[b], Thomas Gheno[c], Nicolas Vanderesse[d], Walid Jomaa[a], Philippe Bocher[a]

[a]*Mechanical engineering department, École de technologie supérieure (ETS), 1100 Rue Notre-Dame Ouest, H3C 1K3 Montréal, Québec, Canada*

bInstitut Clement Ader (ICA) - UMR CNRS 5312, Universit´e de Toulouse, CNRS, INSA, UPS, Mines Albi, ISAE-SUPAERO, Campus Jarlard, 81013 Albi Cedex 09, France

[c]*DMAS, ONERA, Université Paris Saclay, 92322 Chatillon, France*

[d]*PACEA - UMR CNRS 5199, Université de Bordeaux, 33615 Pessac Cedex, France*

Abstract

The paper demonstrates how defects inherited from the deposition processes can severely impair the lifetime of MCrAlY coatings in service.The oxidation behavior of two NiCoCrAlY coatings was investigated at 1150 $^{\circ}$C up to 500 hours. The coatings had the same nominal composition but were processed by two different projection techniques: air plasma spray (APS) and high velocity oxy fuel (HVOF). Freestanding coating specimens were extracted from the coated system and thinned down to different thicknesses ranging from 400 to 15 μm in order to investigate size effects inherent to the oxidation response. The oxidation rate of the APS coating was found to be insensitive to the specimen thickness, while that of the HVOF coating increased with the specimen thickness, due to greater intersplat oxidation. APS specimens thinner than 60 μm experienced intrinsic chemical failure (InCF) due to Al consumption to form the Al_2O_3 scale. In comparison, HVOF specimens with a thickness of 367 μm were subject to InCF after 250-350 hours oxidation. This first stage of InCF resulted in the formation of a Cr_2O_3 layer at the Al_2O_3 /metal interface once Al activity in the MCrAlY coating was low enough to thermodynamically allow Cr_2O_3 to form. In addition, thick HVOF specimens developed mechanically induced chemical

* Corresponding author

Email address: damien.texier@mines-albi.fr (Damien Texier)

failure (MICF) resulting in the formation of $(Ni,Co)(Cr,Al)_2O_4$ spinels on top of the Al_2O_3 scale and within oxide intrusions. The occurrence of MICF was associated with the concomitant effects of Al consumption due to intrusive oxidation and the spallation of the external Al_2O_3 scale.

Keywords: Oxidation MCrAlY coating, Ultrathin samples, Reservoir effect, Intrinsic chemical failure, Mechanically induced chemical failure

1. INTRODUCTION

Structural materials operating at high temperature, such as Ni-based superalloys, are generally coated with MCrAlY (where M = Ni, Co or Ni/Co) or aluminide coatings to improve their protective resistance in severe environmental conditions [1–4]. MCrAlY coatings are widely applied to components exceeding 850 °C, such as first and second stage turbine blades and nozzle guide vanes, compressors, turbine shrouds. They are richer in Al (and Cr) than superalloy substrates, which promotes the formation of a continuous, slow-growing, compact and adherent α-Al_2O_3 scale at temperatures above $\sim$ 1000 °C [5, 6]. The consumption of Al due to both oxide growth and interdiffusion with the substrate [6–9] is central to the system lifetime, as it determines the integrity of the protective Al_2O_3 scale, and thus the delay until faster-growing oxides develop. The "Al reservoir" available in the coating can become a critical factor in aeronautical applications, where coating thicknesses are limited due to weight concerns.

MCrAlY coatings can be manufactured using various techniques depending on the geometry of the substrate to be overlaid [10]. On the one hand, electroplating and electro-codeposition routes have the advantage of producing dense and oxide-free coatings on complex shapes because of their non-line-of-sight deposition capability [8, 11, 12]. For instance, CrAlY-based powders can be codeposited into a (Ni, Co) matrix during the electroplating process. Appropriate post-plating heat treatments are then applied to allow for element interdiffusion between CrAlY-based particles and the matrix. This operation confers mechanical properties to the particle/matrix structure and forms the final MCrAlY microstructure. However, this deposition quality comes at the expense of the process price and productivity [10, 13]. Line-of-sight deposition techniques, such as APS and HVOF deposition processes, are much more affordable

and demonstrate a very interesting trade-off between a cost-efficient process and excellent protection for various industrial applications. However, these projected coatings are much more prone to internal defects such as unmelted particles, pores, internal oxides and/or nitrides, intersplats. Oxygen ingress along these open channels causes oxide intrusions within the coating [14–31]. This oxide intrusion, concomitant to external oxide scale growth, participates in the Al consumption. Therefore, the capability of the coating to form a continuous Al_2O_3 scale, which depends on the available Al reservoir, might be affected by the defect morphology (volume fraction, connectivity). Oxide intrusions were also found to participate in the coating swelling due to the Pilling-Bedworth ratio higher than 1 for Al_2O_3-forming MCrAlY alloys [26]. Oxidation-assisted swelling of the coating generates tensile stress in the external scale, which may lead to scale cracking and spalling [29].

Thermal and environmental conditions can vary depending on the application of the coated components. Maximal temperatures of 1100-1150 °C are generally encountered for MCrAlY coatings, covered or not with a ceramic top coat for thermal barrier coatings (TBC) applications. The formation of the Al_2O_3 scale and intrusions, together with the interdiffusion with the substrate, causes aluminum depletion in the coating. In thin products, this may bring the Al concentration down to a critical level where Al_2O_3 is no longer stable [30, 32–39]. Other oxides may then form at the oxide/gas and metal/oxide interfaces on large regions. This evolution of the protective Al_2O_3 scale is called intrinsic chemical failure (InCF [34]) and is not necessarily associated with an increase of the mass gain [30, 33, 35, 38]. Mechanical, thermal cyclic and thermal transient loading promotes mechano-chemical coupling and the onset of early strain- and oxidation-assisted damage and cracking/spallation of the external oxide scale [40–42]. Repeated through-thickness cracking and/or spallation of the protective Al_2O_3 scale may bring the Al concentration in the vicinity of the oxide spalled and cracked region to a critical healing level. In comparison with InCF, this change in oxidation behavior is local: *i.e.*, where the damage of the oxide scale occurs. This phenomenon is called mechanically induced chemical failure (MICF [34]) and favors the rapid growth of oxides of the base elements (Ni, Co) [6, 43, 44]. Localized and generalized Al_2O_3 failure are highly detrimental to the integrity of the coating itself, and even more damaging in TBC systems. Indeed, fast growing oxides at the bond-coat/top-coat interface may cause the top-coat to spall, thereby exposing the metal parts to excessive temperatures [18,

45]. The integrity of the coated system comes from its native protection against environmental stresses through the Al_2O_3 formation and its long-term chemical stability. Therefore, investigating the Al_2O_3 failure for coated components is central for high temperature applications.

In the present study, oxidation experiments were conducted at 1150 °C on ultrathin freestanding NiCoCrAlY coating specimens extracted from Air Plasma Spray (APS) and High Velocity Oxy Fuel (HVOF)-processed plates. The ultrathin specimens were prepared with a dedicated precision jig [46] in order to activate InCF for short-term high temperature exposures due to through-thickness Al depletion. Interrupted oxidation tests were performed to document the onset and progression of the generalized breakaway as a function of the exposure time. Thermogravimetric analyses were conducted to study the mass variation associated with the formation of the oxidation products. The sensitivity to InCF was evaluated for both types of coatings and the macroscopic oxidation behavior was related to the oxide intrusion. Xray micro computed tomography (micro-CT) and cross-sectional characterizations were conducted in order to assess the proportion of oxide intrusion in comparison with external scale. In order to document the intrusive oxidation within APS and HVOF materials, the oxidation behavior and lifetime of both the projected materials were directly compared to the ones of a "defect-free" cast material with a similar chemical composition solely developing and external Al_2O_3 scale (see specimen UT2 in Ref. [38] for additional information on the microstructure, oxidation behavior and lifetime).

2. EXPERIMENTAL PROCEDURES

2.1. Material

NiCoCrAlY coatings were deposited by HVOF and APS processes on 304 stainless steel (SS) plates with dimensions of $2 \times 50 \times 250$ mm^3. Both coatings were deposited by PRAXAIR Surface Technologies for this specific investigation. The NiCoCrAlY powder used in the present study was provided by PRAXAIR © (NI-191-4 powder). The powder diameter was about 45 ± 10 μm and its chemical composition is given in Table 1. Coatings with a thickness of 600 μm and 1 mm were deposited on the SS plates with the APS and HVOF processes, respectively. On the one hand, debonding occurred during the thermal spray deposition for the APS coating. Therefore,

free-standing coatings samples (FSCS) were naturally obtained with this process. On the other hand, HVOF coatings were adherent even for coating thicknesses of 1 mm. Rectangular samples were then cut with a precision cutting machine and the SS substrate was mechanically ground to roughly obtain 800 ± 50 μm-thick HVOF FSCS.

The FSCS were heat-treated at 1080 °C for 8 hours and then at 870 °C for 20 hours to reproduce the post-deposition heat treatments that are routinely applied to improve the coating adhesion to the substrate by interdiffusion and consequently to optimize the mechanical properties of Ni-based superalloy substrates [47]. Neither was required here, but a standard heat-treatment was nonetheless conducted to generate coating microstructures representative of service conditions.

Table 1: Nominal composition of the NI-191-4 powder used to deposit the NiCoCrAlY coating (in at. % and wt. %)

Element	Ni	Co	Cr	Al	Y
x_i (at. %)	Balance	18.8	16.5	23.0	0.3
w_i (wt. %)	Balance	22.0	17.0	12.3	0.5

The microstructure of the APS and HVOF NiCoCrAlY coatings is illustrated in Fig. 1.It contained β and γ phases with surface fractions about 58% and 42%, respectively (surface fractions obtained from image analyses). The β and γ phases appear in dark and light gray in BSE mode, respectively (see Fig. 1). The microstructure of the APS and HVOF coatings presents features typical of thermal sprayed materials: melted and resolidified powder particles, unmelted powder particle, pores, dispersed alumina oxides and resolidified splats. Both surface and cross-sectional observations evidenced higher occurrence of unmelted powder particles for the HVOF coating (21 ± 2 % using image analysis) for these deposition conditions compared to APS coating (5 ± 2 %). The presence of unmelted powder particles is not related to the deposition process itself but to the chosen process parameters, *e.g.* the powder temperature, velocity, projection distance etc. [15]. While the APS coating depicts a typical microstructure of high temperature projected coatings, the HVOF coating exhibits a rather cold processed microstructure.

Figure 1: Microstructure obtained with a SEM in a BSE mode of the APS and HVOF coatings after standard heat treatment: (a) and (b) Top view observations of the samples (normal to the projection direction), (c) to (f) Cross-sectional (CS) observations of the samples showing melted and resolidified powder particles, unmelted powder particle, pores, dispersed alumina oxides and resolidified splats.

2.2. Thin sample preparation

APS and HVOF FSCS were thinned down with a home-built precision Jig paired with a BUEHLER© grinding/polishing machine to obtain thin samples with different thicknesses. A particular care was paid on the precision jig stability to achieve low thickness variations over centimeter-size samples. The thinning procedure is fully detailed in Refs [46, 48]. Samples with thickness ranging between 400 and 15 μm with less than $\pm$ 3 μm in thickness variation were prepared. A surface finishing of P4000 SiC grit paper was applied on each sample face. In addition, both the projected materials were compared to a cast material with a similar chemical composition but exempt from process-defects (see specimen UT2 in Ref. [38] for additionnal information).

2.3. High temperature oxidation

Thicknesses were measured using a micrometer with an uncertainty of $\pm$ 1 μm, samples were photographed using a calibrated binocular magnifying glass (Leica DMS 300) to document the sample surface and measure the actual surface S. After preparation, samples were cleaned with acetone then ethanol using ultrasonic bath. Sample masses were measured with a precision balance (Sartorius MC5), with a precision of $\pm$ 1.0×10^{-6} g. Samples were weighed three times before and after some oxidation period allowing the mass gain $\Delta m(t)/S$ to be quantified.

Oxidation experiments were conducted at 1150 °C using interrupted furnace tests in a Nabertherm N 11/H furnace in laboratory air (no forced convection) for a cumulative time of up to 500 hours. One sample was used for each thickness condition. Interruptions were done to observe local changes in the oxidation behavior, *e.g.* Al_2O_3 failure and oxide spallation. Samples were vertically hung on alumina supports using holders made of platinum wire during oxidation tests.

Samples were weighed and observed using optical microscopy (OM) at different interruptions: after 5, 10, 15, 20, 50, 100, 150, 250, 350, and 500 cumulative hours. Optical observations aimed at capturing Al_2O_3 failure, *i.e.* new oxidation products either on top of the external oxide scale or at the α-Al_2O_3 /metal interface owing to the semi-transparency of the α-Al_2O_3 scale in the visible spectrum.

2.4. Material characterization

Surface and cross-sectional observations of the oxidized samples were conducted using optical microscopy (OM) and scanning electron microscopy (SEM) in BSE mode. SEM observations were conducted using a Nova NanoSEM 450 field-emission gun SEM (FEG-SEM) from Thermo Fischer Scientific and a JSM 7800F Prime FEG-SEM from JEOL for cross-sectional observations.

Optical observations were performed to quantitatively document oxide intrusion in the different materials using laser scanning confocal microscopy (Olympus LEXT OLS5100). Automatic stitching in laser intensity mode was conducted to cover large regions of interest with a resolution compatible with the oxide thickness (external oxide scale and oxide intrusion). The whole cross-section was imaged for each sample to analyze sample length compatible with the sparsely distributed intrusive oxide for the APS coating reported in a previous study [29]. Images were thus segmented using *Fiji* [49] in order to dissociate the oxide intrusion from the external oxide and the remaining metal.

CT-scans were performed on thick samples of APS and HVOF coatings oxidized for 500 h to quantitatively document oxide intrusion in three dimensions. Two slabs with dimensions $1\times2\times0.2$ mm^3 and $1\times2\times0.4$ mm^3 were cut from the APS and HVOF samples, respectively. They were characterized with a v tome xs 240 scanner (GE) equipped with a DXR250 detector (2024×2024 $pixels^2$ with a dimension of 200×200 μm^2). The scanning parameters were as follows: numerical resolution: 1.75 μm /voxel, voltage: 100 kV, intensity: 180 μA, exposure time: 1 s, filter: 0.1 mm thick Cu plate, 3 frames averaging, 2550 projections for 360 $^\circ$ rotation. The projections were processed with the program *Phoenix datos—x reconstruction 2*. After reconstruction, the 3D images were analyzed with *Dragonfly 2021.3* [50]. The images were segmented using the Otsu algorithm, enabling a quantitative and localized analysis of the intruded

oxides within the matrix.

3. RESULTS

3.1. Mass gain evolution

Mass gain evolution was investigated for both the APS and HVOF coatings up to 250 cumulative hours for all the coating samples, as depicted in Fig. 2. The oxidation behavior of a cast material with a similar chemical composition was added as a green dashed curve on the different graphs for direct comparison with a material without projection defects (results from Ref. [38]). On the one hand, the mass gain of the APS coating was found nearly insensitive to the sample thickness and matched well with the one of the cast material. For short oxidation duration, the mass gain is slightly higher for the APS material in comparison with the cast material. The oxidation rate follows a power law with an exponent close to 3 similarly to the cast materials, as observed on the log-log representation. More details on the oxidation of the APS coatings are reported in Ref. [30]. On the other hand, the mass gain evolution of the HVOF coating was found particularly sensitive to the specimen thickness. Thick samples demonstrate a greater mass gain for all the oxidation duration. For instance, the mass gain of the 367 μm-thick HVOF specimen after 250 hours is nearly 9 times greater than the one of the cast material. Interestingly, the oxidation rate of the HVOF samples follows also a power law with an exponent close to 3 regardless of the specimen thickness (parallel linear trends in Fig. 2d). In addition, the three thinnest HVOF specimens and the thinnest APS sample have a decrease in oxidation rate after 100 hours.

Figure 2: Mass gain evolution at 1150 $^\circ$C for both the APS and HVOF free-standing coating specimens with various thicknesses: (a) and (c) Δm/S versus time representations, (b) and (d) log-log representations. The oxidation behavior of the cast material with a similar chemical composition was added as a green dashed curve on the different graphs for direct comparison (results from Ref. [38]).

The oxidation kinetics were analyzed with a power law:

$$\left(\frac{\Delta m}{S}\right)^n = k_n \cdot t \tag{1}$$

where Δm is the mass gain, S is the external surface area, n and k_n and the oxidation exponent and constant, respectively, and t is the time. Values of n and k_n fitted on the mass gain data are reported as a function of the specimen thickness in Fig. 3. The average value of the exponent was found to be 3.5 $\pm$ 0.6 for APS sample and 3.4 $\pm$ 0.4 for the HVOF ones. While k_n is insensitive to the thickness for the APS coating with a value of 6.9×10^{-3} $\pm$ 5.7×10^{-3} $\mathrm{mg}^{3.5}.\mathrm{cm}^{-7}\,\mathrm{s}^{-1}$ (with n=3.5), its value increases with the thickness for the HVOF coating from 1.0×10^{-3} $\mathrm{mg}^{3.5}.\mathrm{cm}^{-7}\,\mathrm{s}^{-1}$ to 4.2×10^{0} $\mathrm{mg}^{3.5}.\mathrm{cm}^{-7}\,\mathrm{s}^{-1}$ (with n=3.5).

Figure 3: Evolution of the (a) oxidation rate exponent n and (b) oxidation constant k_n as a function of the specimen thickness.The oxidation behavior of the cast material with a similar chemical composition was added as a green dashed curve on the different graphs for direct comparison (results from Ref. [38]).

3.2. Evolution of the oxide scale

Macrographs were recorded for both the APS and HVOF materials at each interruption (Fig. 4). After 5 hour oxidation, all the specimens have a homogeneous and continuous light gray aspect, corresponding to the stable Al_2O_3 external oxide scale. For the APS coating, darker regions appear after 20 and 100 hours on the 24 and 33 μm-thick specimens, respectively. These darker regions, highlighted with green arrows in Fig. 4, correspond to the onset of InCF, as reported in Refs. [30, 38]. Specimens with a thickness of 61 μm or greater did not experience any InCF. For the HVOF coating, InCF was found to occur after 20 hours on the 15 μm-thick specimen. Interestingly, Al_2O_3 failure was observed for all the specimens for oxidation duration lower than 250 hours regardless of the specimen thickness (and even 150 hours for specimens thinner than 200 μm).

Figure 4: Macrographs showing surface evolution for both the APS and HVOF coatings at different oxidation cumulative time and specimen thicknesses. Green arrows highlight the onset of InCF. Please see the high-resolution version of the present figure for better details on InCF events. Partly reprinted from Corrosion Science, 184, Texier et al., Screening for Al_2O_3 failure in

MCrAlY APS coatings using short-term oxidation at high temperature, 109334-4, Copyright (2021), with permission from Elsevier [30].

Oxide spallation was found to occur for both materials (light gray regions in Figs. 4 and 5). It became significant after 50 hours, and was more important in thicker samples. Thick APS coatings developed an external oxide scale with a homogeneous gray level (except oxide spalled regions) up to 500 hours, corresponding to Al_2O_3 formation. Interestingly, thick HVOF coatings developed an external oxide scale with blueish islets spreading onto the surface. Blue oxide was mainly observed in regions where Al_2O_3 spalled at the previous cooling step (see *e.g.* supplementary materials Fig. S1). This local change in oxidation behavior preceded by Al_2O_3 spallation is consistent with MICF. Due to the increasing sensitivity to Al_2O_3 spallation with increasing specimen thickness, more than 10 % of the sample surface is covered by MICF at 250 hours and 150 hours for specimens thinner and thicker than 150 μm, respectively. The blueish oxide scale covers the majority of the specimen surface after 350 hours. While the APS specimens were only prone to InCF, HVOF specimens can be subject to InCF and MICF simultaneously. It is also important to note that specimens thinner than 30 μm did not experience any oxide spallation and were solely sensitive to InCF. In addition, the oxide scale was less prone to spall once InCF or MICF developed.

Figure 5: Surface macrographs of a 238 μm-thick APS and a 367 μm-thick HVOF coating samples, showing the evolution of oxide spallation and the development of the blue oxide.

3.3. Cross-sectional observations

Cross-sectional observations were conducted on the APS and HVOF coatings after 250 hour cumulative oxidation exposure for thick and thin samples, as illustrated in Figs. 6 and 7 respectively. Oxide intrusions were found in both materials, but extended deeper and developed thicker patterns in the HVOF coating. These intrusive oxides formed in intersplat and unmelted particle regions. For the APS coating, thin oxide stringers are observed and thick oxide intrusions are sparsely distributed on the cross-section views. Both the thick oxide intrusions and thin oxide stringers were characterized as Al_2O_3 using energy dispersive X-Ray (EDX) analyses. Some

AlN precipitates were also observed within the bulk of APS coatings inherited from the deposition process (see Ref. [30] for additional information). $(Ni,Co)(Cr,Al)_2O_4$ spinels developed above the external Al_2O_3 scale but also in the specimen bulk of some HVOF specimens in the core of sub-surface intrusive oxides (white arrows showing lighter gray regions in the core of Al_2O_3 intrusions in Fig. 6(d)). These spinels were mainly found in a shallow region beneath and connected to the external oxide scale. The spinel formation was not necessarily associated with an advanced consumption of aluminum within the metallic material. These $(Ni,Co)(Cr,Al)_2O_4$ spinels were observed in regions of HVOF specimens with a β-γ microstructure in the specimen core. EDS analyses on the 200- and 367-μm thick HVOF specimens revealed a large variability in Al content from regions to regions but Al content as high as 24 at.% was found far from regions developing $(Ni,Co)(Cr,Al)_2O_4$ spinels.

In addition, a slight undulation of the surface was observed for thick HVOF samples, especially in the vicinity of sub-surface oxide intrusions. This undulation might result from growth stresses associated with the formation of the intense intrusive oxides. The Al_2O_3 would expand more than the metal it consumes to form the intrusive oxides (Pilling-Bedworth ratio of Al_2O_3 in Ni-based alloys nearly 1.8 [51]), thus deforming the material.

Figure 6: Cross-sectional observations of thick-samples after 250 hours at 1150 $^\circ$C showing difference in intrusive oxidation for a (a) 520 μm, (c)200 μm, (e)140 μm-thick APS and a (b) 367 μm, (d) 367 μm, (f) 367 μm-thick HVOF coatings.

Cross-sectional observations of thin specimens experiencing InCF at 1150 $^\circ$C for 250 hours are depicted in Fig. 7. For thin APS coatings, a $(Cr,Al)_2O_3$ layer was found to develop at the Al_2O_3 /metal interface and CrN particles also formed in this region. For thin HVOF coatings, similar $(Cr,Al)_2O_3$ layer grew at the Al_2O_3 /metal interface but $(Ni,Co)(Cr,Al)_2O_4$ spinels developed in the core of Al_2O_3 intrusions, as a second stage to InCF. This second stage of InCF, was not associated with a full consumption of Cr in the bulk of HVOF coatings.

Figure 7: Cross-sectional observations of thin-samples after 250 hours at 1150 °C showing difference in intrinsic chemical failure (InCF) for 24 µm-thick APS and 25 µm-thick HVOF coatings.

Cross-sectional observations of thick specimens after 500 hours exposure at 1150 °C are depicted in Fig. 8. Al_2O_3 remained stable for the APS samples while $(Ni,Co)(Cr,Al)_2O_4$ oxides were observed as a continuous external layer for the HVOF samples, without the formation of the $(Cr,Al)_2O_3$ layer at the Al_2O_3 /metal interface. $(Ni,Co)(Cr,Al)_2O_4$ oxides also formed in the core of intrusive oxides only for the HVOF samples even for the thickest samples (367 µm). $(Ni,Co)(Cr,Al)_2O_4$ spinels within intrusive oxides developed at depths shorter than 60 µm, *i.e.* at a depth less than 1.5 CrAlYTa particle size.

Figure 8: Cross-sectional observations of thick samples after 500 hours at 1150 °C showing difference in external oxide scale composition between APS and HVOF coatings.

3.4. Quantitative analyses of the intrusive oxidation

Large cross-sectional observations and CT-scans were investigated in order to dissociate the contribution of the external oxide scale and the oxide intrusion after 500 h at 1150 °C in two and three dimensions, respectively. While solely the thickest samples were investigated via tomographic observations, different samples thicknesses ranging from 55 to 367 µm were analyzed using cross-sectional observations. Illustrations of the 3D macrographs are depicted in *"supplementary materials" (Figs. S2 to S6)*. Intrusive oxides were thus segmented for both 2D and 3D characterizations to quantify their fraction and distribution within the sample and the fraction of intrusive oxidation compared to the external oxide scale. Segmented surfaces of the external oxide scale (S_{ext}), of oxide intrusions (S_{int}) and of the metallic region (S_{met}) were illustrated in *"supplementary materials" (Fig. S7)*.

As aforementioned, intrusive oxides were segmented and compared to the external oxide scale, as shown by the S_{int}/S_{ext} ratio in Fig. 9(a). Both surface ratio (solid markers) and volume ratio (blank markers), respectively obtained from cross-sectional views and 3D CT-Scan results,

were plotted for direct comparison. For the APS samples, the surface/volume occupied by intrusive oxides was found slightly lower than the one of the external oxide scale (S_{int} / S_{ext} ratio less than 1). The dark gray horizontal dashed line illustrates the $S_{int} = S_{ext}$ condition. For HVOF samples, the contribution of intrusive oxides is greater and the S_{int} / S_{ext} ratio increased with the sample thickness. Indeed, the surface occupied by intrusive oxides was more than ten times greater than the external oxide surface for the 367 μm-thick HVOF sample after 500 h at 1150 $^{\circ}$C. Therefore, the contribution of oxide intrusions to the mass gain of the HVOF samples is further demonstrated, and explains the observed effect of the sample thickness on the oxidation kinetics. In addition, the fraction of intrusive oxide within the metallic material was considered as the cross-sectional surface (or volume from CT-scans) of intrusive oxide S_{int} divided by the cross-sectional surface (volume) of the sample except the surface (volume) of the external surface (S_{met}). Please refer to *"supplementary materials" (Fig. S7)* for illustration of S_{int} and S_{met}. Similarly, V_{int} and V_{met} are considered using 3D CT-Scan results. The fraction of intrusive oxide within the metallic material for the whole samples was depicted in Fig. 9(b). This fraction was roughly constant, regardless of the sample thickness for both the APS and HVOF materials. After 500 h at 1150 $^{\circ}$C, the intrusive oxide occupied 8 and 35 % of the metallic sample for the APS and HVOF materials, respectively. 2D cross-sectional (CS) and 3D CT-scans (CT-S) results are consistent.

Figure 9: Evolution of the surface fraction of intrusive oxidation as a function of the sample thickness for both the APS and HVOF coatings after 500 hours at 1150 $^{\circ}$C. (a) Comparison with the external oxide, (b) comparison with the metallic material.

Oxide segmentation also aimed to evaluate the distribution of intrusive oxidation within the bulk of the metallic material. The fraction of intrusive oxide within the metallic material was calculated at different locations from the center of the sample, as illustrated in Fig. 10. The profile of the intrusive oxidation fraction across the sample thickness has a "U"-shape regardless of the sample thickness and deposition process. The external oxide scale is not represented in this graph. Intrusive oxidation was greater in a shallow region beneath the external oxide scale then the

fraction decreased in the sample core. Interestingly, fractions of intrusive oxidation greater than 40 % were reported for both materials. This fraction decreased to a core value of nearly $4 \pm 3\%$ and $24 \pm 3\%$ for the APS and HVOF materials, respectively. Cross-sectional and CT-scan results were also consistent.

Figure 10: Distribution of the fraction of intrusive oxidation within the metallic material across the sample thickness for both the APS and HVOF after 500 hours at 1150 $^{\circ}$C. The external oxide scale is not represented in this graph.

4. DISCUSSION

The comparison between the high temperature oxidation of APS and a HVOF coatings with similar nominal composition provides an opportunity to document how processed-inherited features affect the oxidation behavior, *i.e.* mass gain evolution and oxide formation, and ultimately the lifetime. Both projected materials developed an external oxide scale together with intrusive oxidation along intersplats and around unmelted particles, with a greater sensitivity for the HVOF coating. The greater sensitivity to intrusive oxidation is not attributed to the HVOF process but to the particular process parameters for the HVOF deposition used in the present paper. The comparison between APS and HVOF materials with the cast material with a similar chemical composition gives the opportunity to document the oxidation behavior when solely external oxidation takes place [38], and provide an opportunity to discuss on the contribution of oxide intrusions on InCF, MICF, and lifetime, *i.e.* time to Al_2O_3 failure.

4.1. Origin of intrusive oxidation

As aforementioned, APS and HVOF materials developed intrusive oxidation along intersplats and around unmelted particles. Intrusive oxidation was found more pronounced on the HVOF material due to a high fraction of unmelted particles (see *e.g.* Fig. 1). Intrusive oxidation was reported for different MCrAlY projected coatings, with a sensitivity not clearly associated to a deposition process [14–31]. For instance, several authors reported that HVOF MCrAlY coatings were less prone to intrusive oxidation compared to APS (or even low pressure plasma spraying (LPPS)) [20, 23, 25]. The sensitivity to intrusive oxidation was found to be related to the presence

and interconnection of unmelted powder particles. Process parameters such as powder temperature and velocity play a significant role on the fraction of unmelted powder particles in projected materials [15]. Hotter process conditions for this specific HVOF material could improve its oxidation resistance and lifetime. Intersplat regions also participate in intrusive oxidation but in a less extensive manner due to morphological aspects. Intersplat regions for the APS material are more likely found orthogonal to the projection direction, *i.e.* orthogonal to the oxygen ingress direction / inward oxygen flux. The lack of adhesion of unmelted particles in the HVOF material generates continuous channels, whereas intersplat regions appear more discontinuous (see *e.g.* Fig. 1). Therefore, defect connectivity from particles to particles seems greater for materials having unmelted particles, especially in depth, as depicted in Figs. 1.(c) and (d). This particular defect morphology favors oxide intrusion in depth, thus affecting the core of the projected material due to deep open porosity. With these specific process conditions, the APS material is more likely to have closed porosity while the HVOF materials has a greater open porosity. Oxidation of intersplat regions and/or unmelted particles can be significantly limited using additional surface treatments to close pores and channels [52].

4.2. Effect of intrusive oxidation on the Al_2O_3 failure

The motivation of the present paper is not to discriminate a deposition process but to investigate intrusive oxidation related to process-inherited defects and ultimately its lifetime based on the Al_2O_3 failure. Both external oxidation and intrusive oxidation participate in the mass gain evolution and in the consumption of metallic elements participating in the oxide formation. Different kinetics of oxidation and oxides in presence were found for the APS and HVOF materials due to the much more severe intrusive oxidation for the HVOF process. Two different oxidation mechanisms were reported to participate for the Al_2O_3 failure depending on the specimen thickness: (i) the intrinsic chemical failure (InCF) due to aluminum consumption, and (ii) the mechanically induced chemical failure (MICF) due to oxide spallation. These oxidation mechanisms are dependant on the specimen thickness since thin specimens are sensitive to reservoir effects and thick specimens are more prone to oxide spallation. Therefore, the competition between both the oxidation mechanisms will be discussed below for the APS and HVOF materials and compared to the cast material.

Based on the Pilling-Bedworth ratio of the metal/oxide system, development of oxide intrusions leads to swelling of the material or at least put the metal in a complex stress state. Such volume expansion can contribute to spallation of the external oxide scale, as observed in Ref. [30] and can participate in the development of the intrusive oxidation. However, the coatings developed oxide intrusions before scale spallation started. Therefore, scale spallation was not the primary cause for intrusive oxidation.

APS materials with a thickness greater than 60 μm developed Al_2O_3 as external and intrusive oxides for samples up to 500 hours. Despite oxide spallation, APS materials did not experience MICF in the time/temperature window. Samples as thin as 60 μm were necessary to activate InCF for the APS coating at 1150 $^\circ C$ up to 500 hours oxidation, as depicted in Fig. 4 (time to InCF = 20 and 100 hours for 24 and 33 μm-thick APS specimens). InCF was found associated with the formation of a Cr_2O_3 layer and CrN precipitates at the Al_2O_3 /metal interface (See *e.g.* Fig.7 and Ref. [30] for more details). Similar results were reported for the cast material experiencing solely external oxidation, as reported in Ref. [38]. InCF resulted in the formation of a Cr_2O_3 layer at the Al_2O_3 /metal interface without precipitation of CrN. The cast materials experienced InCF after 20 and 200 hours for 11 and 26 μm-thick specimens, respectively. These longer time to Al_2O_3 failure arise from the absence of intrusive oxidation, thus limiting the aluminum consumption compared to the APS material.

For the HVOF material, both InCF and MICF were observed in competition depending on the specimen thickness. Severe intrusive oxidation and oxide spallation for the HVOF material impaired the stability of Al_2O_3. A continuous $(Ni,Co)(Cr,Al)_2O_4$ spinel layer developed on top of the Al_2O_3 scale and within intrusive Al_2O_3 for specimens thicker than 55 μm (Fig. 6). This second stage of oxidation is associated with the blueish coloration of HVOF samples. $(Ni,Co)(Cr,Al)_2O_4$ islets formed and spread from regions subjected to oxide spallation at previous interruptions (see *e.g.* supplementary materials, Fig. S1). The formation of $(Ni,Co)(Cr,Al)_2O_4$ spinels on top of the Al_2O_3 scale corresponds to MICF and was not associated with a particular increase in the oxidation rate due to the continued presence of the slow-diffusing oxide [33, 35–37, 53]. While both APS and HVOF materials were subject to Al_2O_3 spallation, solely HVOF formed large regions of $(Ni,Co)(Cr,Al)_2O_4$ spinels for

specimens with thickness ranging from 55 to 367 μm. Meng et al. reported similar formation of $(Ni,Co)(Cr,Al)_2O_4$ spinels on top of the external Al_2O_3 scale after isothermal oxidation of an APS MCrAlY alloys developing severe oxide intrusion at intersplat regions [27, 28]. In addition to MICF, InCF occurred for HVOF specimens regardless of the specimen thickness in this temperature-time window. Specimen as thick as 367 μm developed InCF since the fraction of intrusive oxides was found 10 times greater than the one of the external oxide scale (Figs. 2 and 9). Both InCF and MICF were observed for HVOF specimens thicker than 55 μm while thinner specimens were only sensitive to InCF due to lack in oxide spallation. Therefore, both oxide spallation and oxide intrusion are central in the Al_2O_3 failure and lifetime of thin MCrAlY products.

4.3. Influence of oxide intrusion on the lifetime of projected MCrAlY materials

In an attend to predict the lifetime of material investigated in the this work, the analytical model previously described in Refs. [30, 38] is used. The assumption of flat diffusion profiles and mass balance equilibrium allows the analytical estimation of the Al concentration in the metallic MCrAlY as a function of the mass gain and thus the time. Time to InCF can thus be considered as the time necessary to consume all the Al content from the MCrAlY alloy due to external and intrusive oxidation. The model is based on the hypotheses detailed below:

- Composition profiles are nearly flat due to fast diffusion in both γ and β phase, relative to the oxidation rate;
- The quantity of non-oxidized elements, *i.e.* Co, Cr and Ni, remains constant in the metallic alloy during the Al_2O_3 growth stage;
- The alloy molar volume is considered constant;
- The specimen creep due to oxide growth is negligible;
- The kinetics of oxidation for the external and intrusive oxidation are comparable due to the open porosity associated to intersplat/unmelted particles regions.

The time to failure t_{InCF} can thus be expressed as follow (see Refs. [30, 38]:

$$t_{InCF} = \frac{1}{k_n}\left(\frac{3 \cdot M_O}{4 \cdot M_{Al}} \cdot \rho_{MCrAlY} \cdot \xi_{MCrAlY} \cdot w_{Al}\right)^n \quad (2)$$

with M_{O} and M_{Al} the molar mass of O and Al, $\rho_{\mathrm{Al_2O_3}}$ the density of $\mathrm{Al_2O_3}$, ξ_{MCrAlY} the thickness of the coating sample, and w_{Al} the weight fraction of Al in the MCrAlY alloy. Both model and experimental data were compared in Fig. 11. For the HVOF material, k_{n} was found to increase with the specimen thickness and can be expressed as a power law function of the specimen thickness (see *e.g.* Fig. 3(b)). Dashed lines correspond to the time to InCF for all the materials and colored domains correspond to time-thickness domain for which InCF is supposed to occur. While the time to InCF rapidly increases for the APS and cast materials for specimens thicker than 30 μm, time to InCF for HVOF specimens was found to linearly and slowly increase with the specimen thickness. For the experimental results, specimens covered by at least 10 % by InCF or MICF were considered as affected by InCF or MICF, respectively. Both experiments and models were found to particularly match for the APS material. For the HVOF materials, the model tends to slightly overestimate the time to InCF for thick specimens. It is worth mentioning that oxide spallation at the different interruption was not considered both in the experimental mass gain measurement and in the model, leading to faster consumption of Al. The distribution of oxide intrusion might also play a role on the local consumption of Al within the metallic MCrAlY alloy due to presence of residual β precipitates when both InCF and MICF occurred for thick HVOF specimens.

Figure 11: Lifetime prediction of the MCrAlY alloy as a function of the specimen thickness at 1150 °C for the APS, the HVOF and the cast materials.

5. CONCLUSION

The oxidation behavior of two projected NiCoCrAlY coatings, *i.e.* APS and a HVOF coatings, was investigated using thin freestanding specimens exposed at 1150 °C up to 500 hours. A large amount of unmetled particules led to severe oxide intrusion for the HVOF coatings. The main differences in oxidation behavior for both the coatings consist in:

- A greater mass gain for the HVOF coating condition investigated here compared to the APS coating and the model material;
- A mass gain increasing with the coating thickness for the HVOF coating due to severe

oxide intrusion via oxygen transport through intersplat channels. The oxide intrusion was found more severe in the extreme surface compared to the specimen bulk due to oxygen transportation and/or diffusion via the intersplat channels. The oxidation rate of the APS coating was found insensitive to the specimen thickness as long as no intrinsic chemical failure (InCF) occurred. For APS coatings, the oxide intrusion was less pronounced and mainly connected to the external oxide scale;

- A greater sensitivity to oxide spallation for the HVOF coating, especially for thicker samples;
- A greater sensitivity to intrinsic chemical failure (InCF) for the HVOF coating. The first stage of InCF, *i.e.* the Al_2O_3 failure to form Cr_2O_3 and/or CrN at the Al_2O_3 /metal interface, occurred for thin APS specimens (samples thinner than 60 μm) and for all the HVOF samples (samples as thick as 367 μm) in the time/temperature window. A second stage of InCF resulting in the formation of $(Ni,Co)(Cr,Al)_2O_4$ spinels as an external oxide scale and within oxide intrusion occurred for all the HVOF samples.

It is worth noting that defects inherited from the deposition processes severely impair the oxidation resistance and lifetime of MCrAlY coatings under service. In the present study, the HVOF coating experienced a poor oxidation resistance compared to the APS coating. However, other deposition parameters could inverse this trend. The prediction of InCF occurrence based on the deposition process parameters and/or non-destructive analyses of microstructure is needed to better estimated the lifetime of coating system due to oxidation and interdiffusion. Additional surface treatments preventing oxygen transportation within intersplat channels could improve the reactivity of such projected coatings.

6. AKNOWLEDGEMENTS

This work was supported by the Agence Nationale de la Recherche (ANR) [ANR-18-CE08-0003; ANR-JCJC-COMPAACT project funded from the AAPG2018].

7. DATA AVAILABILITY

The raw/processed data required to reproduce these findings cannot be shared at this time due to technical or time limitations.

References

[1] R. Mévrel, State of the art on high-temperature corrosion-resistant coatings, Materials Science and Engineering: A 120-121 (1989) 13–24.

[2] T. Rhys-Jones, Coatings for blade and vane applications in gas turbines, 1989. doi: 10.1016/0010-938X(89)90104-2.

[3] S. Bose, High temperature coatings, 1st ed. ed., Butterworth-Heinemann, 2007. doi: 10.1016/B978-0-7506-8252-7.X5000-8.

[4] J. Nicholls, Designing oxidation-resistant coatings, JoM 52 (2000) 28–35.

[5] H. Evans, M. Taylor, Oxidation of high-temperature coatings, Proceedings of the Institution of Mechanical Engineers, Part G: Journal of Aerospace Engineering 220 (2006) 1–10.

[6] W. Sloof, T. Nijdam, On the high-temperature oxidation of MCrAlY coatings, International Journal of Materials Research 100 (2009) 1318–1330.

[7] N. Vialas, D. Monceau, Effect of Pt and Al content on the long-term, high temperature oxidation behavior and interdiffusion of a Pt-modified aluminide coating deposited on Ni-base superalloys, Surface and Coatings Technology 201 (2006) 3846–3851.

[8] A. Raffaitin, D. Monceau, E. Andrieu, F. Crabos, Cyclic oxidation of coated and uncoated single-crystal nickel-based superalloy MC2 analyzed by continuous thermogravimetry analysis, Acta Materialia 54 (2006) 4473–4487.

[9] M. Elsaß, M. Frommherz, A. Scholz, M. Oechsner, Interdiffusion in MCrAlY coated nickel-base superalloys, Surface and Coatings Technology 307 (2016) 565–573.

[10] Y. Tamarin, Protective coatings for turbine blades, ASM international, 2002.

[11] Y. Zhang, An Alternative Low-Cost Process for Deposition of MCrAlY Bond Coats for Advanced Syngas/Hydrogen Turbine Applications, Technical Report, Tennessee Technological University, 2015. URL: https://www.osti.gov/biblio/1253139. doi: 10.2172/1253139.

[12] D. Texier, D. Monceau, F. Crabos, E. Andrieu, Tensile properties of a non-line-of-sight processed β - γ - γ ' MCrAlY coating at high temperature, Surface and Coatings Technology 326 (2017) 28–36.

[13] D. Tejero-Martin, M. Rezvani Rad, A. McDonald, T. Hussain, Beyond traditional coatings: A review on thermal-sprayed functional and smart coatings, Journal of Thermal

Spray Technology 28 (2019) 598–644.

[14] Characterization of plasma sprayed and electron beam-physical vapor deposited thermal barrier coatings, volume 4 of *Turbo Expo: Power for Land, Sea, and Air*, 1997. doi: 10.1115/97-GT-531.

[15] A. Léger, J. Wigren, M. Hansson, Development of a process window for a NiCoCrAlY plasma-sprayed coating, Surface and Coatings Technology 108-109 (1998) 86–92.

[16] P. Niranatlumpong, C. Ponton, H. Evans, Failure of protective oxides on plasma-sprayed NiCrAlY overlay coatings, Oxidation of Metals 53 (2000) 241–258.

[17] F. Belzunce, V. Higuera, S. Poveda, High temperature oxidation of HFPD thermal-sprayed MCrAlY coatings in simulated gas turbine, Materials Science and Engineering A 297 (2001) 162–167.

[18] H. Evans, M. Taylor, Diffusion cells and chemical failure of MCrAlY bond coats in thermal-barrier coating systems, Oxidation of Metals 55 (2001) 17–34.

[19] W. R. Chen, X. Wu, B. R. Marple, P. C. Patnaik, Oxidation and crack nucleation/growth in an air-plasma-sprayed thermal barrier coating with NiCrAlY bond coat, Surface and Coatings Technology 197 (2005) 109–115.

[20] M. Shibata, S. Kuroda, H. Murakami, M. Ode, M. Watanabe, Y. Sakamoto, Comparison of microstructure and oxidation behavior of conicraly bond coatings prepared by different thermal spray processes, MATERIALS TRANSACTIONS 47 (2006) 1638–1642.

[21] T. Patterson, A. Leon, B. Jayaraj, J. Liu, Y. Sohn, Thermal cyclic lifetime and oxidation behavior of air plasma sprayed conicraly bond coats for thermal barrier coatings, Surface and Coatings Technology 203 (2008) 437–441.

[22] D. Seo, K. Ogawa, Y. Suzuki, K. Ichimura, T. Shoji, S. Murata, Comparative study on oxidation behavior of selected MCrAlY coatings by elemental concentration profile analysis, Applied Surface Science 255 (2008) 2581–2590.

[23] P. Richer, M. Yandouzi, L. Beauvais, B. Jodoin, Oxidation behaviour of CoNiCrAlY bond coats produced by plasma, HVOF and cold gas dynamic spraying, Surface and Coatings Technology 204 (2010) 3962–3974.

[24] K. Ma, J. Schoenung, Isothermal oxidation behavior of cryomilled NiCrAlY bond coat : Homogeneity and growth rate of TGO, Surface & Coatings Technology 205 (2011) 5178–5185.

[25] L. Wang, Y. Zhao, X. Zhong, S. Tao, W. Zhang, Y. Wang, Influence of “island-like” oxides in the bond-coat on the stress and failure patterns of the thermal-barrier coatings fabricated by atmospheric plasma spraying during long-term high temperature oxidation, Journal of Thermal Spray Technology 23 (2014) 431–446.

[26] J. Jiang, Z. Zou, W. Wang, X. Zhao, Y. Liu, Z. Cao, Effect of internal oxidation on the interfacial morphology and residual stress in air plasma sprayed thermal barrier coatings, Surface and Coatings Technology 334 (2018) 215–226.

[27] G.-H. Meng, B.-Y. Zhang, H. Liu, G.-J. Yang, T. Xu, C.-X. Li, C.-J. Li, Highly oxidation resistant and cost effective MCrAlY bond coats prepared by controlled atmosphere heat treatment, Surface and Coatings Technology 347 (2018) 54–65.

[28] G.-H. Meng, H. Liu, M.-J. Liu, T. Xu, G.-J. Yang, C.-X. Li, C.-J. Li, Highly oxidation resistant MCrAlY bond coats prepared by heat treatment under low oxygen content, Surface and Coatings Technology 368 (2019) 192–201.

[29] D. Texier, C. Cadet, T. Straub, C. Eberl, V. Maurel, Tensile behavior of air plasma spray MCrAlY coatings: Role of high temperature agings and process defects, Metallurgical and Materials Transactions A 51 (2020) 2766–2777.

[30] D. Texier, M. Ecochard, T. Gheno, D. Monceau, M. Salem, P. Lours, Screening for al2o3 failure in mcraly coatings using short-term oxidation at high temperature, Corrosion Science 184 (2021) 109334.

[31] H. Chen, M. Fan, L. Li, W. Zhu, H. Li, J. Li, Y. Yin, Effects of internal oxide contents on the oxidation and β-phase depletion behaviour in HOVF CoNiCrAlY coatings, Surface and Coatings Technology 424 (2021) 127666.

[32] D. Whittle, Spalling of protective oxide scales, Oxidation of Metals 4 (1972) 171€”179.

[33] K. Ishii, M. Kohno, S. Ishikawa, S. Satoh, Effect of rare-earth elements on high-temperature oxidation resistance of Fe-20Cr-5Al alloy foils, Materials transactions 38 (1997) 787–792.

[34] H. Evans, A. Donaldson, T. Gilmour, Mechanisms of breakaway oxidation and application to a chromia-forming steel, Oxidation of Metals 52 (1999) 379–402.

[35] G. Strehl, D. Naumenko, H. Ai-Badairy, L. Rodriguez Lobo, G. Borchardt, G. Tatlock, W. Quadakkers, The effect of aluminium depletion on the oxidation behaviour of FeCrAl foils, Materials at High Temperatures 17 (2000) 87–92.

[36] D. Young, A. Chyrkin, W. Quadakkers, A simple expression for predicting the oxidation limited life of thin components manufactured from FCC high temperature alloys, Oxidation of Metals 77 (2012) 253–264.

[37] D. Young, A. Chyrkin, J. He, D. Grüner, W. Quadakkers, Slow transition from protective to breakaway oxidation of haynes 214 foil at high temperature, Oxidation of Metals 79 (2013) 405–427.

[38] T. Gheno, C. Rio, M. Ecochard, D. Texier, Alumina failure and post-failure oxidation in the nicocraly alloy system at high temperature, Oxidation of metals 96 (2021) 487–517.

[39] C. Romain, D. Texier, C. Desgranges, J. Cormier, S. Knittel, D. Monceau, D. Delagnes, Oxidation of thin nickel-based superalloy specimens: Kinetics study and mechanical integrity, Oxidation of Metals 96 (2021) 169–182.

[40] H. Hindam, D. P. Whittle, Microstructure, adhesion and growth kinetics of protective scales on metals and alloys, Oxidation of Metals 18 (1982) 245–284.

[41] H. E. Evans, Stress effects in high temperature oxidation of metals, International Materials Reviews 40 (1995) 1–40.

[42] T. Pollock, B. Laux, C. Brundidge, A. Suzuki, M. He, Oxide-assisted degradation of Ni-base single crystals during cyclic loading: the role of coatings, Journal of the American Ceramic Society 94 (2011) s136–s145.

[43] C. Giggins, F. Pettit, Oxidation of Ni-Cr-Al Alloys Between 1000° and 1200°C, Journal of The Electrochemical Society 118 (1971) 1782–1790.

[44] J. Wilber, M. Bennett, J. Nicholls, Life-time extension of alumina forming FeCrAI-RE alloys: Influence of alloy thickness, Materials at High Temperatures 17 (2000) 125–132.

[45] E. P. Busso, H. E. Evans, Z. Q. Qian, M. P. Taylor, Effects of breakaway oxidation on local stresses in thermal barrier coatings, Acta Materialia 58 (2010) 1242–1251.

[46] D. Texier, D. Monceau, J.-C. Salabura, R. Mainguy, E. Andrieu, Micromechanical testing of ultrathin layered material specimens at elevated temperature, Materials at high temperatures 33 (2016) 325–337.

[47] D. Texier, D. Monceau, Z. Hervier, E. Andrieu, Effect of interdiffusion on mechanical and thermal expansion properties at high temperature of a MCrAlY coated Ni-based superalloy, Surface and Coatings Technology 307 (2016) 81–90.

[48] D. Texier, Measurement and Evolution of the gradient of mechanical properties in

MCrAlY coated MC2 nickel based superalloy system, Dissertation, UniversitÃ© de Toulouse, Toulouse, 2013. URL: doi:10.13140.

[49] J. Schindelin, I. Arganda-Carreras, E. Frise, V. Kaynig, M. Longair, T. Pietzsch, S. Preibisch, C. Rueden, S. Saalfeld, B. Schmid, J.-Y. Tinevez, D. White, V. Hartenstein, K. Eliceiri, P. Tomancak, A. Cardona, Fiji: an open-source platform for biological-image analysis, Nature Methods 9 (2012) 676–682.

[50] Object Research Systems (ORS) Inc, Montreal, Canada, Dragonfly 2021.3, 2021. URL: https://www.theobjects.com/dragonfly/.

[51] C. Xu, W. Gao, Pilling-Bedworth ratio for oxidation of alloys, Materials Research Innovations 3 (2000) 231–235.

[52] Y. Wu, G. Zhang, Z. Feng, B. Zhang, Y. Liang, F. J. Liu, Oxidation behavior of laser remelted plasma sprayed NiCrAlY and NiCrAlY-Al_2O_3 coatings, Surface & Coatings Technology 138 (2001) 56–60.

[53] E. Fedorova, D. Monceau, D. Oquab, Quantification of growth kinetics and adherence of oxide scales formed on Ni-based superalloys at high temperature, Corrosion Science 52 (2010) 3932–3942.

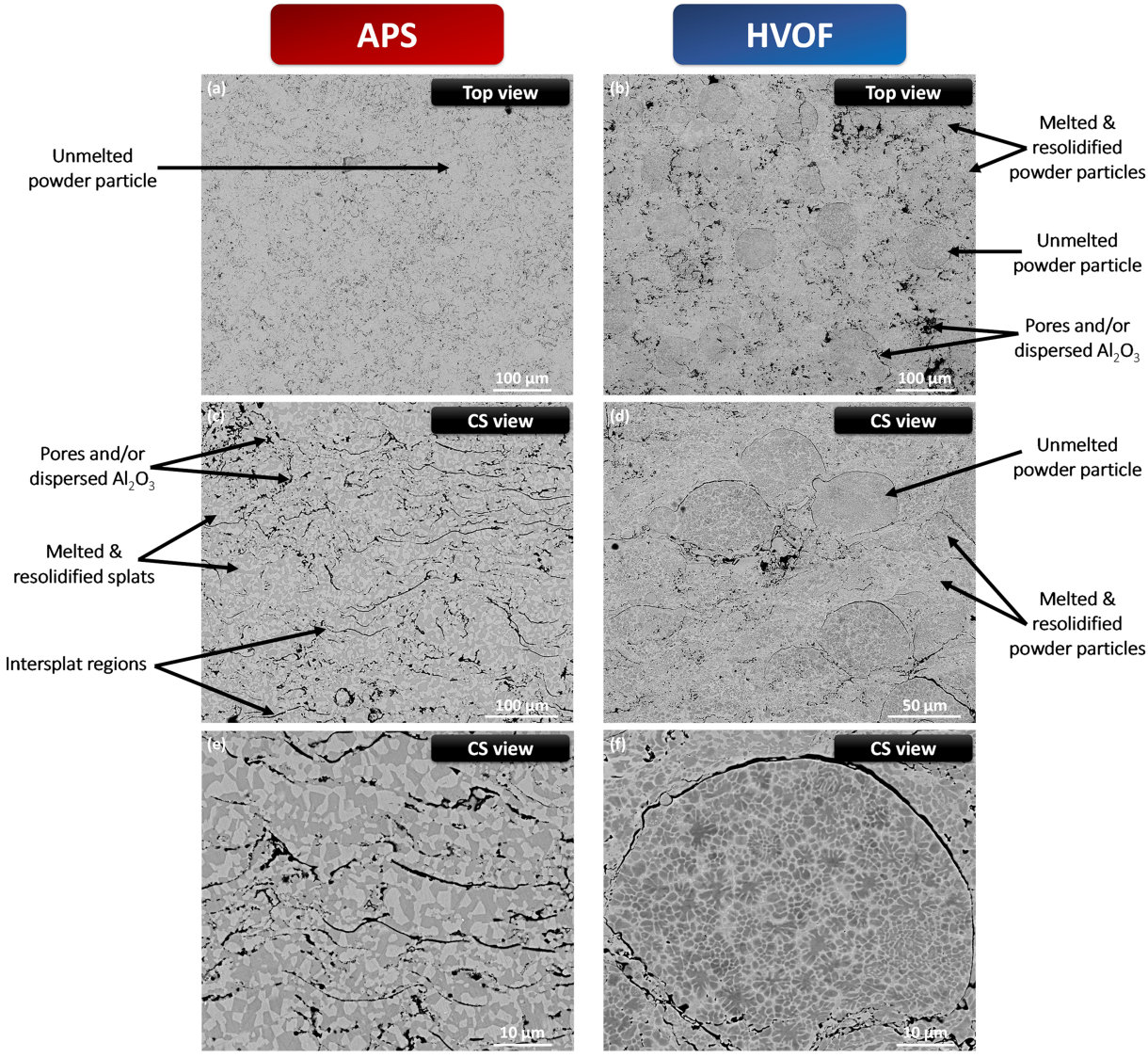
APS
HVOF
(a)
Top view
100 µm
(b)
Top view
100 µm
Unmelted powder particle
Melted & resolidified powder particles
Unmelted powder particle
Pores and/or dispersed Al_2O_3
(c)
CS view
100 µm
(d)
CS view
50 µm
Pores and/or dispersed Al_2O_3
Melted & resolidified splats
Intersplat regions
Unmelted powder particle
Melted & resolidified powder particles
(e)
CS view
10 µm
(f)
CS view
10 µm

Figure 1

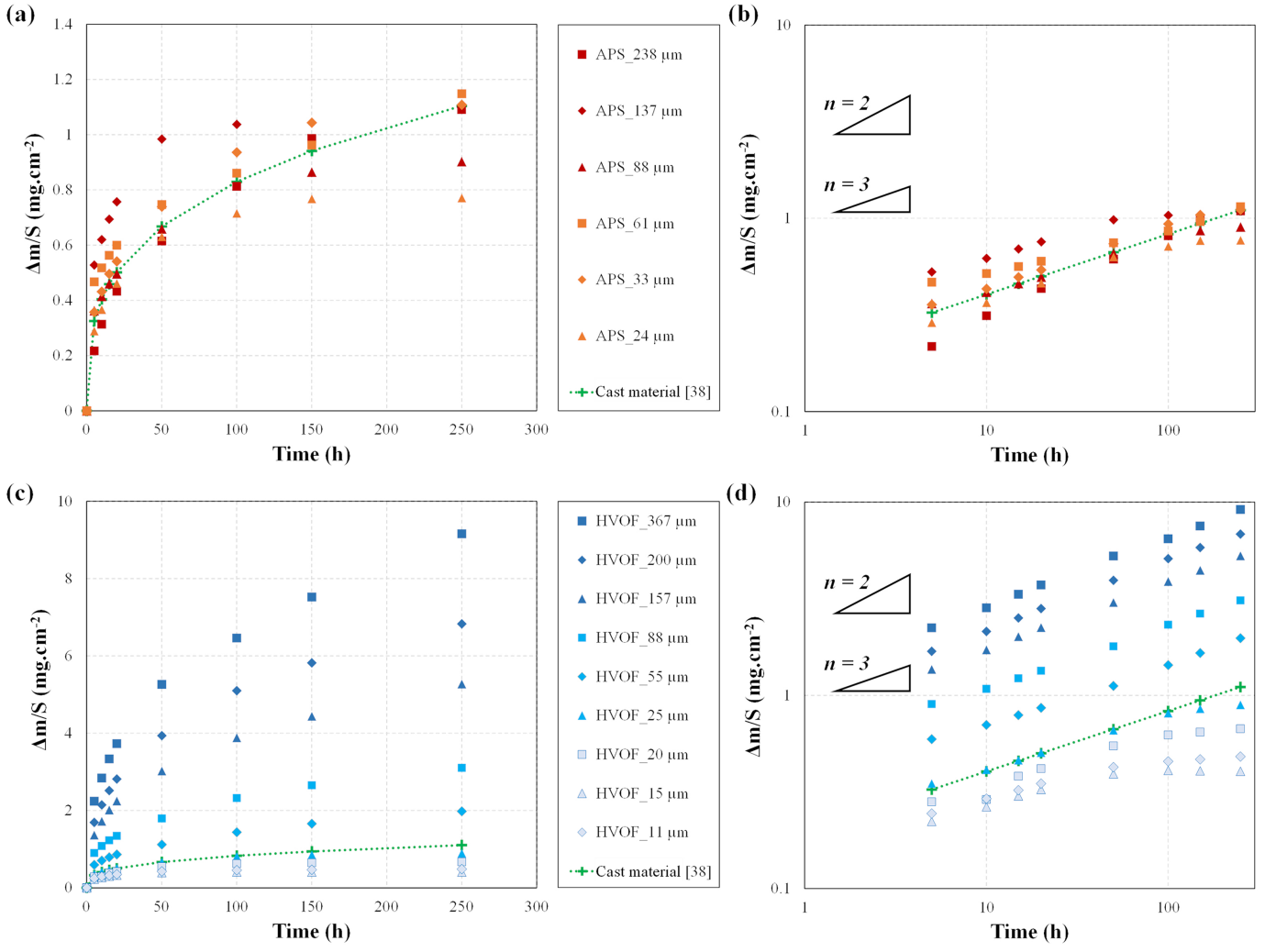
(a)
Δm/S (mg.cm-2)
Time (h)
APS_238 µm
APS_137 µm
APS_88 µm
APS_61 µm
APS_33 µm
APS_24 µm
Cast material [38]
(b)
n = 2
n = 3
Δm/S (mg.cm-2)
Time (h)
(c)
HVOF_367 µm
HVOF_200 µm
HVOF_157 µm
HVOF_88 µm
HVOF_55 µm
HVOF_25 µm
HVOF_20 µm
HVOF_15 µm
HVOF_11 µm
Cast material [38]
Δm/S (mg.cm-2)
Time (h)
(d)
n = 2
n = 3
Δm/S (mg.cm-2)
Time (h)

Figure 2

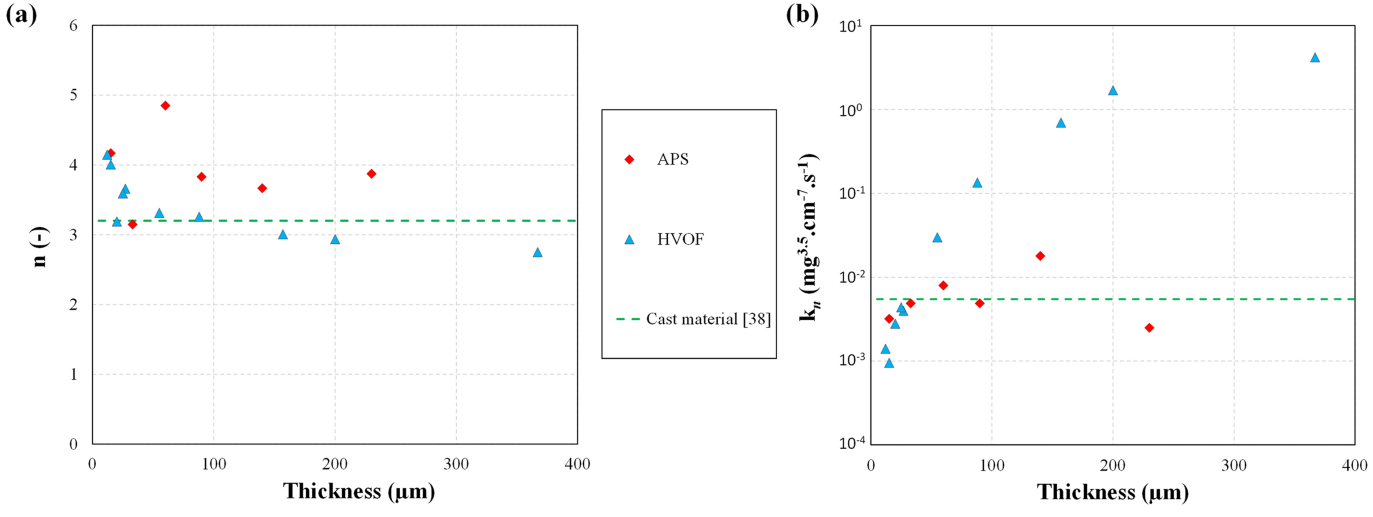
(a)
n (-)
Thickness (µm)
APS
HVOF
Cast material [38]
(b)
k_H (mg$^{3.5}$.cm^{-7}.s^{-1})
Thickness (µm)

Figure 3

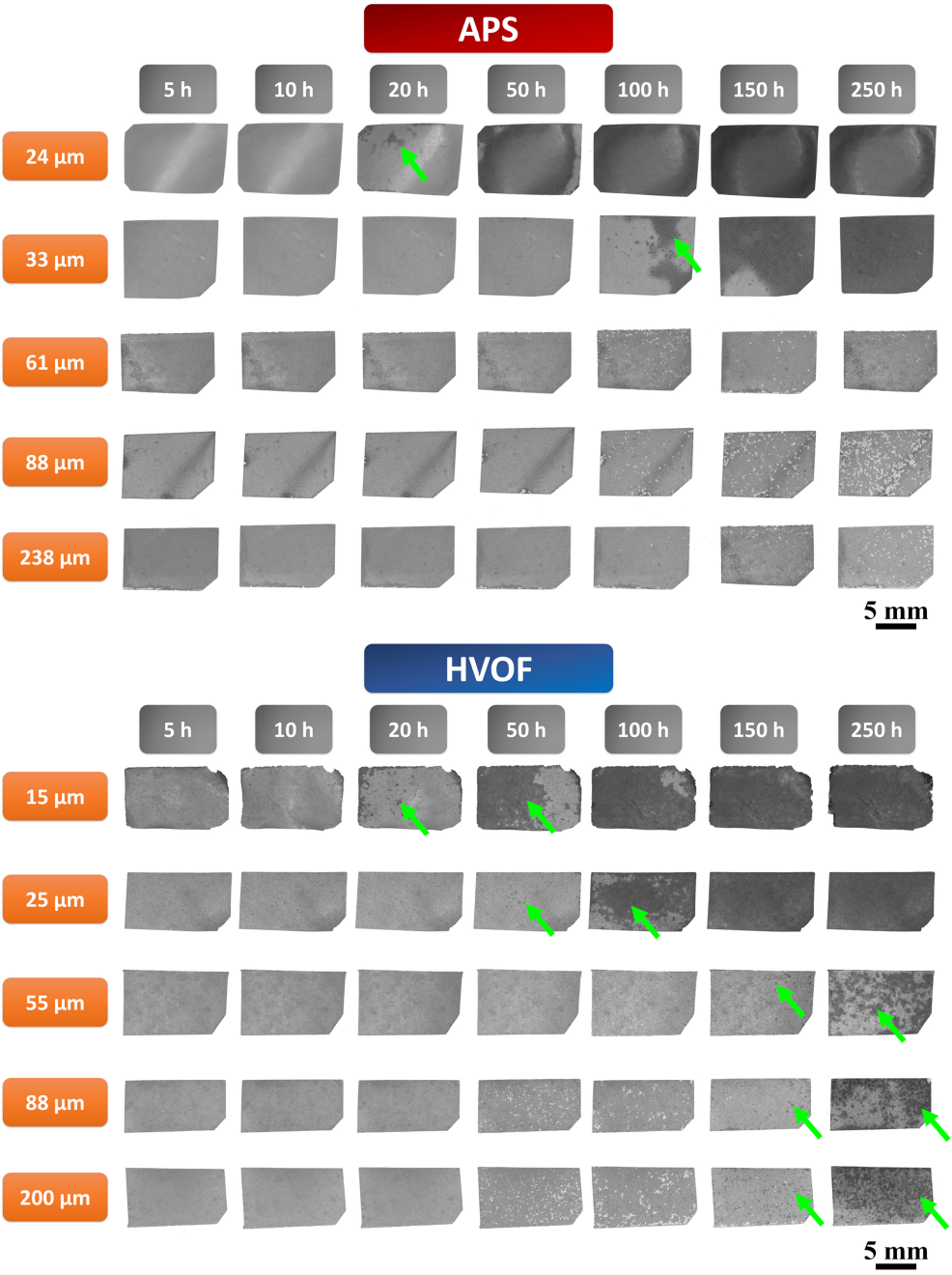
APS
5 h
10 h
20 h
50 h
100 h
150 h
250 h
24 µm
33 µm
61 µm
88 µm
238 µm
5 mm
HVOF
5 h
10 h
20 h
50 h
100 h
150 h
250 h
15 µm
25 µm
55 µm
88 µm
200 µm
5 mm

Figure 4

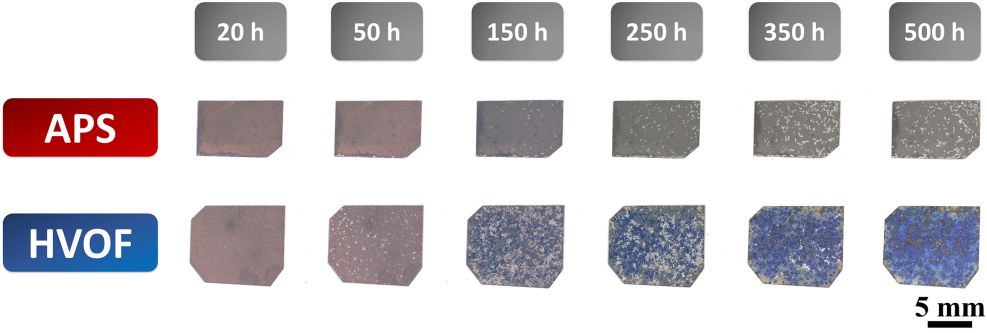

Figure 5

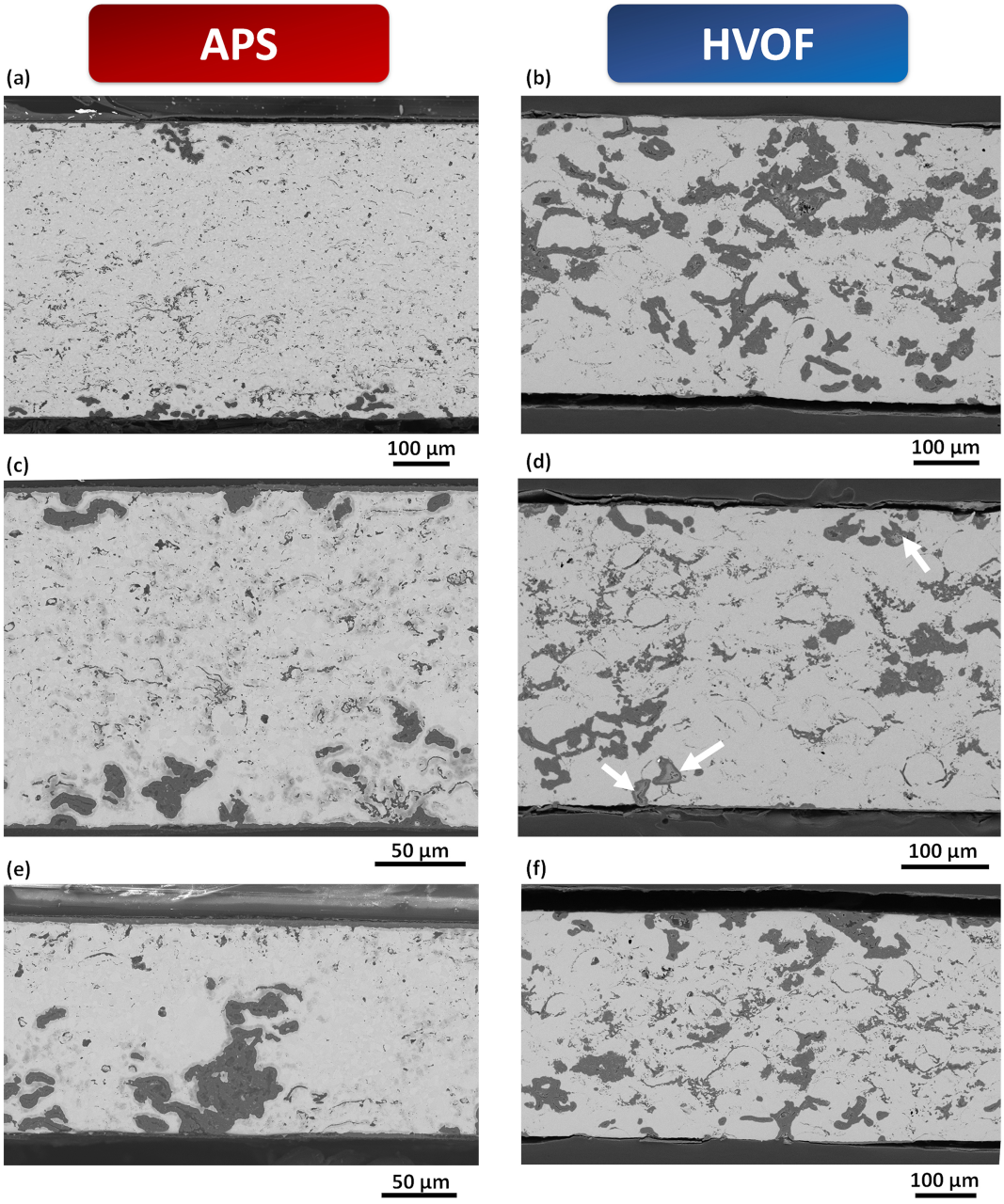

Figure 6

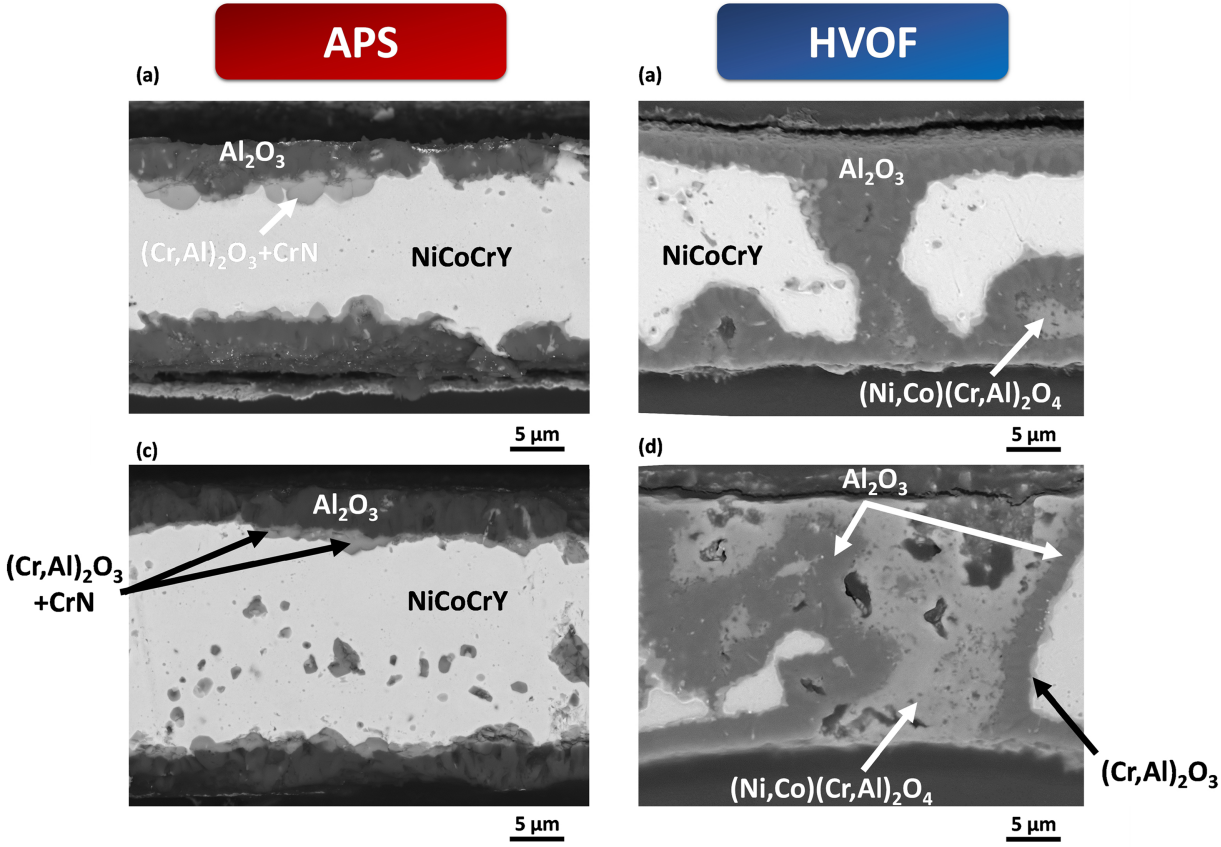
APS
HVOF
(a)
(a)
Al_2O_3
$(Cr,Al)_2O_3$+CrN
NiCoCrY
Al_2O_3
NiCoCrY
$(Ni,Co)(Cr,Al)_2O_4$
5 µm
5 µm
(c)
(d)
Al_2O_3
$(Cr,Al)_2O_3$ +CrN
NiCoCrY
Al_2O_3
$(Ni,Co)(Cr,Al)_2O_4$
$(Cr,Al)_2O_3$
5 µm
5 µm

Figure 7

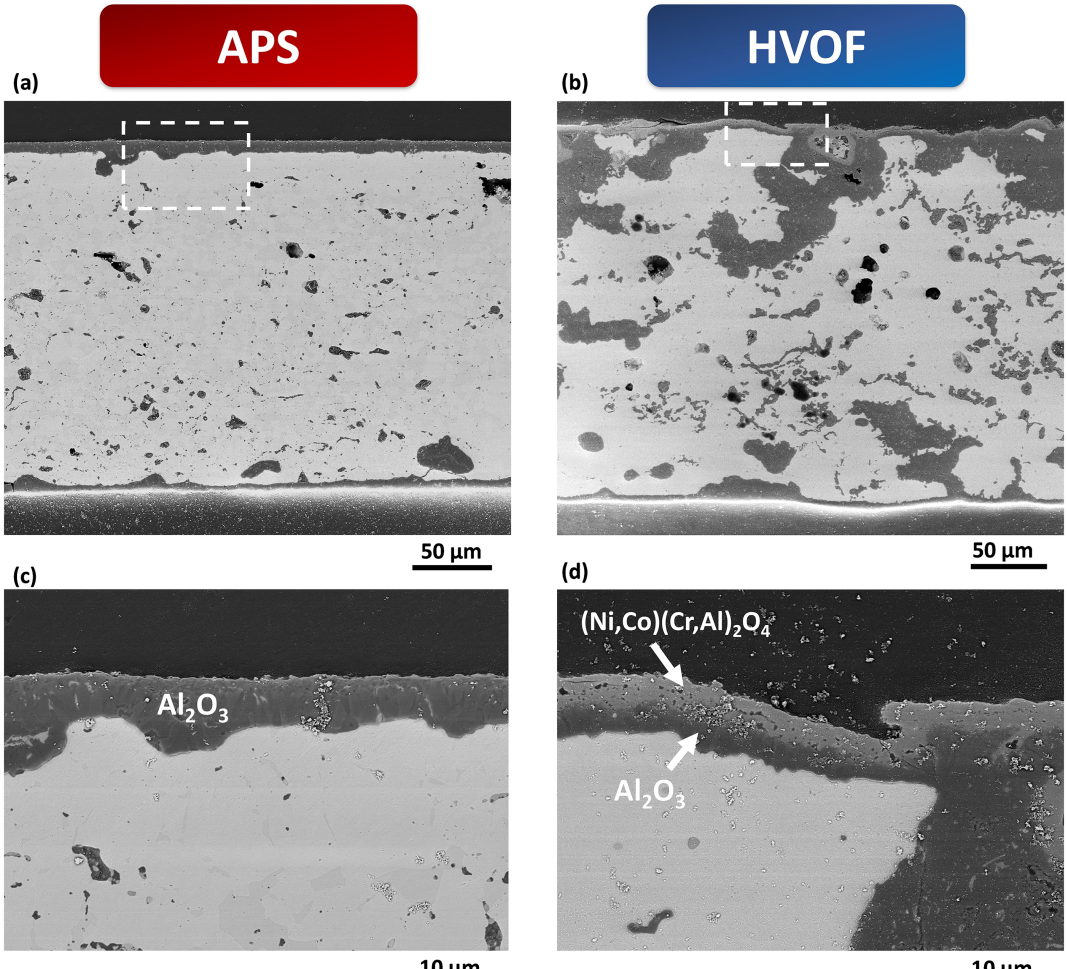

Figure 8

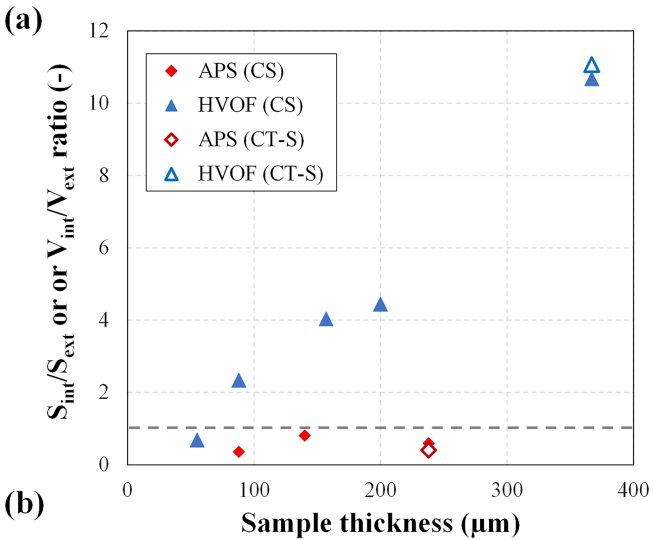
(a)
APS (CS)
HVOF (CS)
APS (CT-S)
HVOF (CT-S)
S_{int}/S_{ext} or or V_{int}/V_{ext} ratio (-)
Sample thickness (µm)
0
2
4
6
8
10
12
0
100
200
300
400

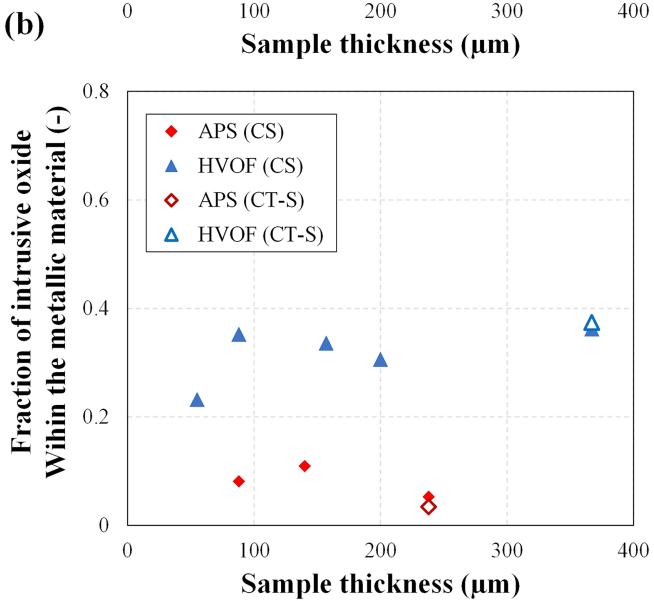
(b)
APS (CS)
HVOF (CS)
APS (CT-S)
HVOF (CT-S)
Fraction of intrusive oxide
Wihin the metallic material (-)
Sample thickness (µm)
0
0.2
0.4
0.6
0.8
0
100
200
300
400

Figure 9

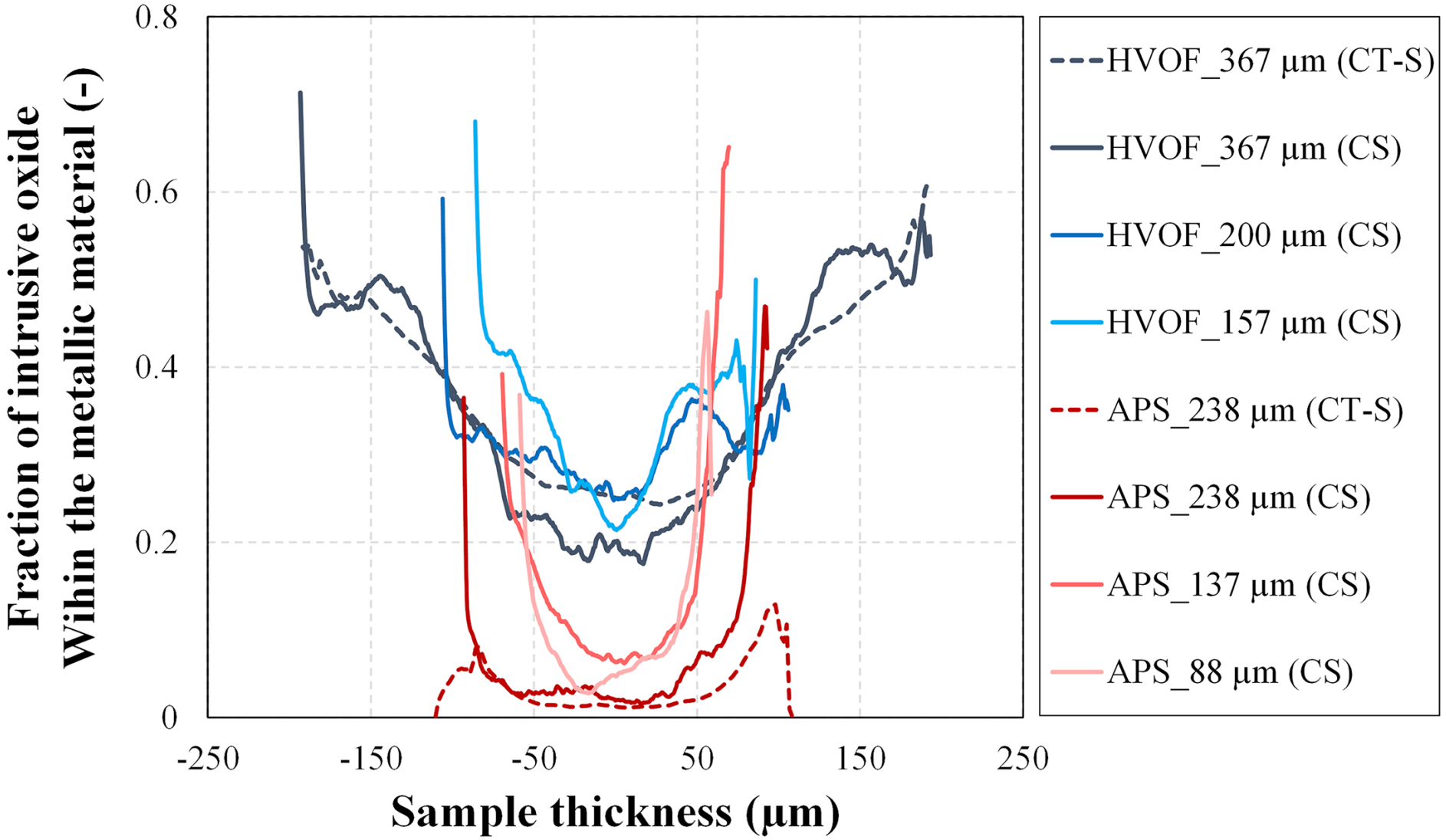
Fraction of intrusive oxide
Wihin the metallic material (-)
0.8
0.6
0.4
0.2
0
-250
-150
-50
50
150
250
Sample thickness (µm)
HVOF_367 µm (CT-S)
HVOF_367 µm (CS)
HVOF_200 µm (CS)
HVOF_157 µm (CS)
APS_238 µm (CT-S)
APS_238 µm (CS)
APS_137 µm (CS)
APS_88 µm (CS)

Figure 10

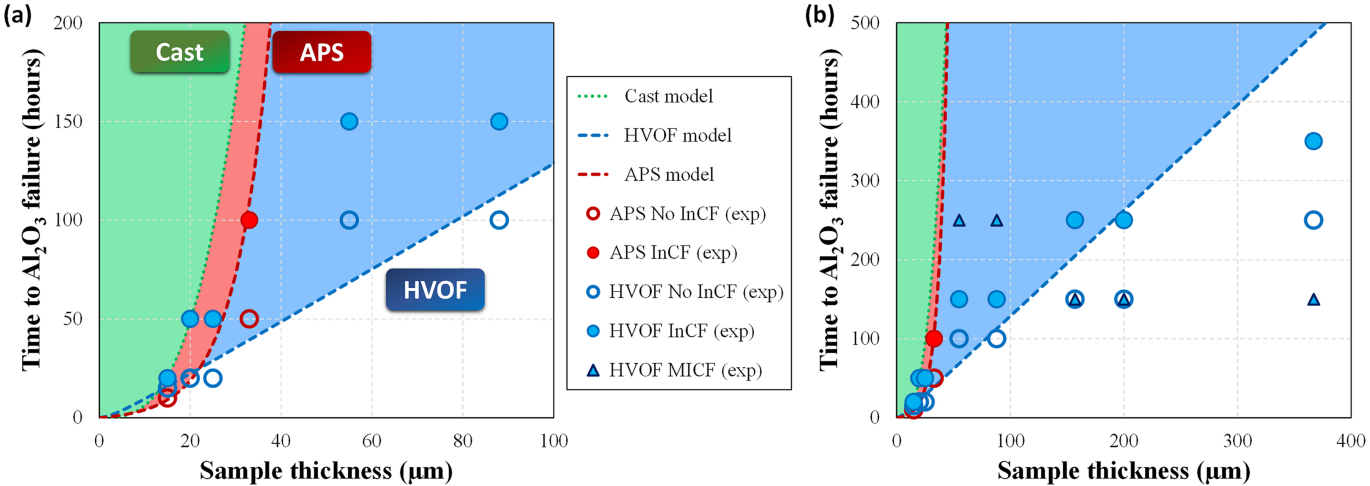
(a)
Cast
APS
HVOF
Time to Al_2O_3 failure (hours)
Sample thickness (μm)
0
50
100
150
200
0
20
40
60
80
100
Cast model
HVOF model
APS model
APS No InCF (exp)
APS InCF (exp)
HVOF No InCF (exp)
HVOF InCF (exp)
HVOF MICF (exp)
(b)
Time to Al_2O_3 failure (hours)
Sample thickness (μm)
0
100
200
300
400
500
0
100
200
300
400

Figure 11